JPhys Materials

PURPOSE-LED PUBLISHING™

PAPER • OPEN ACCESS

Effect of deposition template on high entropy oxide model systems for the oxygen evolution reaction

To cite this article: Iris C G van den Bosch *et al* 2026 *J. Phys. Mater.* **9** 035007

View the article online for updates and enhancements.

You may also like

- Autler–Townes splitting in Rydberg atoms: transition dipole matrix element extraction and field efficiency analysis
Brian C Holloway, Gavin M Chase, Lee E Harrell et al.
- ICRH modelling of DTT in full power and reduced-field plasma scenarios using full wave codes
A Cardinali, C Castaldo, F Napoli et al.
- Co-design and implementation of community-based flood early warning systems in eastern Argentina
Federico Robledo, Diego Moreira, Camila Prudente et al.

This content was downloaded from IP address 158.69.200.216 on 15/11/2026 at 17:41

Journal of Physics: Materials

Check for updates

OPEN ACCESS

RECEIVED
26 April 2026

REVISED
8 June 2026

ACCEPTED FOR PUBLICATION
15 June 2026

PUBLISHED
13 July 2026

Original content from this work may be used under the terms of the Creative Commons Attribution 4.0 licence.

Any further distribution of this work must maintain attribution to the author(s) and the title of the work, journal citation and DOI.

PAPER

Effect of deposition template on high entropy oxide model systems for the oxygen evolution reaction

Iris C G van den Bosch[1], Martina Tsvetanova[1], Melissa J Goodwin[1], Edwin Dollekamp[2], Nini Pryds[2], Gertjan Koster[1] and Christoph Baeumer[1,*]

[1] MESA+ Institute, University of Twente, Drienerlolaan 5, Enschede, 7522 NB, The Netherlands
[2] Technical University of Denmark, Fysikvej 310, 2800 Kgs Lyngby, Denmark
[*] Author to whom any correspondence should be addressed.

E-mail: c.baeumer@utwente.nl

Keywords: high entropy oxides, oxygen evolution reaction, epitaxial thin films, pulsed laser deposition, freestanding thin films, nanosheets

Supplementary material for this article is available online

Abstract

High-entropy oxide catalysts are promising candidates for overcoming intrinsic activity limitations in the oxygen evolution reaction (OER), a key bottleneck in electrochemical conversion. Thin-film model systems provide a controlled platform for uncovering the underlying catalytic mechanisms. Here, we develop and compare four deposition templates for $LaNi_{0.2}Co_{0.2}Fe_{0.2}Mn_{0.2}Cr_{0.2}O_3$ model systems: (i) epitaxial films on $Nb:SrTiO_3$, (ii) sacrificial-layer-released films transferred to platinized Si wafers, (iii) locally epitaxial films grown on oxide nanosheets, and (iv) films directly grown on platinized Si wafers. These geometries support a wide range of operando techniques while enabling direct comparison of materials grown under identical pulsed laser deposition conditions. Using electrochemical measurements and *ex-situ* characterization, we evaluate crystallinity, stoichiometry, surface morphology, and OER activity across the different templates. The observed variations highlight the important role of template selection in interpreting catalytic performance. We find that the transferred epitaxial thin film and the film on $Nb:SrTiO_3$ are comparable in stoichiometry and electrocatalytic activity, while the epitaxial film has higher crystallinity. The films on nanosheets and directly grown on Pt have a reduced crystallinity, broader orientation distribution, different stoichiometry and a lower catalytic activity. Overall, this set of deposition templates facilitates the integration of well-controlled model systems with operando spectroscopy, advancing mechanistic insight and guiding the rational design of next-generation high-entropy OER catalysts.

1. Introduction

The electrochemical splitting of water is widely recognized as a pivotal technology for the global transition toward sustainable energy systems. However, the overall efficiency of water electrolysis is limited by the sluggish kinetics of the oxygen evolution reaction (OER), a complex four-electron transfer reaction. Numerous material systems have been investigated to improve the OER activity, and high-entropy materials, i.e. single phase materials with five or more different elements on the same crystal lattice site, have emerged as a promising platform for catalyst optimization. In fact, both metallic high-entropy alloys and high entropy oxides (HEOs) have demonstrated superior OER activity [1–5]. High-entropy materials possess a multitude of different active sites in close proximity, so that neighboring sites have been speculated to contribute to forming different reaction intermediates, leading to decreased overpotentials [1].

Despite these advances, conventional powder-based catalyst studies remain limited by heterogeneous particle sizes, uncontrolled crystallographic orientations, mixed surface terminations, and morphology-dependent effects. These complexities hinder the establishment of clear structure—property—activity relationships and mechanistic understanding. While such limitations are common to powder catalysts

© 2026 The Author(s). Published by IOP Publishing Ltd

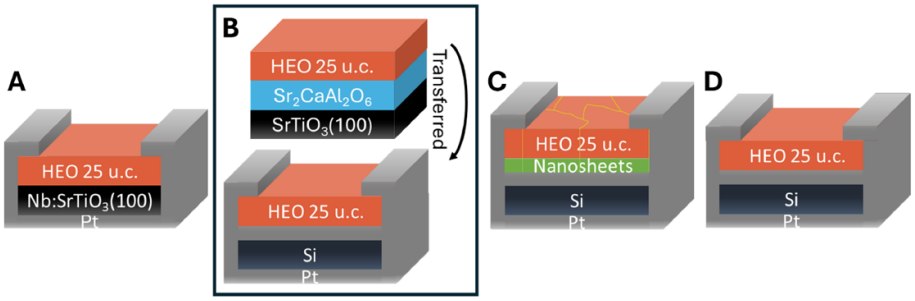


Figure 1. Schematics of HEO thin films on various deposition templates. (A) Nb:$SrTiO_3$, (B) epitaxially grown and transferred to Si \ SiO_2 \ TiO_x \ Pt. (C) Si \ SiO_2 \ TiO_x \ Pt \ $Ca_2Nb_3O_{10}$, (D) Si \ SiO_2 \ TiO_x \ Pt.

in general, they are particularly pronounced in high-entropy oxides, where compositional complexity introduces additional variables that are difficult to disentangle.

To overcome these challenges, the field has increasingly turned to epitaxial thin-film model systems [6–8]. These systems enable precise control of surface orientation, strain, and interfaces, allowing systematic studies of structure–property–activity relationships. Their value is highlighted by recent studies showing that oxides undergo complex surface transformations that strongly influence catalytic behavior, phenomena that are difficult to identify and quantify in powder systems [4, 9–11].

A detailed understanding of these transformations and their impact on OER activity increasingly relies on advanced platforms for (electronic-)structure characterization and mechanistic studies, including operando and *in situ* approaches. Consequently, the field of electrocatalysis is experiencing a rapid shift toward operando optical and x-ray-based spectroscopies and spectro-electrochemical microscopy, supplemented by (usually *ex-situ*) pump–probe methods and advanced electron microscopies. These methods provide insights into oxidation states, metal–oxygen hybridization, covalency, defect formation, surface reconstruction, reaction intermediates, and electrolyte structure during catalytic operation. Operando approaches include measurements through thin liquid layers, like a meniscus [12–14] or using microfluidic flow channels [15]. Techniques that probe through the solid, e.g. using (holey) SiN_x membranes to enable x-ray or photoelectron detection [16–19], thereby minimizing x-ray attenuation by water, are particularly attractive for studying electrochemical interfaces under relevant flow and current density conditions.

Despite these methodological advances, a critical gap remains: operando and advanced mechanistic studies of epitaxial (high-entropy) oxide model systems are still scarce. A central limitation is the lack of versatile, well-controlled thin-film platforms that are simultaneously compatible with epitaxial growth requirements and with the diverse architectural constraints imposed by advanced spectroscopic, microscopic, and time-resolved techniques. Requirements for conductivity, thickness, substrate transparency, and geometric configuration differ substantially across techniques, emphasizing the need for versatile yet well-defined model system platforms.

For growth on x-ray or electron-transparent substrates, which usually prevent epitaxial growth of the catalyst layer, the use of oxide nanosheet seed layers represents an important step toward operando-compatible model catalysts [17, 18]. These nanosheets act as epitaxial templates with lateral dimensions of several micrometers and a thickness of a single unit cell, enabling local epitaxial growth [20]. More recently, freestanding film transfer techniques have emerged as a promising strategy to move from local epitaxial growth with grain boundaries to fabrication of single crystalline films on arbitrary substrates. In this approach, fully epitaxially grown films are released from their growth substrates and transferred onto new supports with millimeter-scale lateral dimensions [21–25], enabling compatibility with substrates such as holey SiN_x membranes. However, this relatively new approach has not yet been widely applied in electrocatalysis applications. Beyond operando compatibility, such freestanding oxides are also of interest for accessing new physics and functionality unique to substrate-decoupled oxide membranes [26–28], which may also open new avenues for tuneable electrocatalysis.

In this work, we address the synthesis and characterization gap of operando-compatible HEO model systems by developing and comparing $LaNi_{0.2}Co_{0.2}Fe_{0.2}Mn_{0.2}Cr_{0.2}O_3$ thin films grown on a set of deposition templates. We investigate four distinct sample geometries (figure 1): (A) epitaxial single-crystalline HEOs grown on Nb:$SrTiO_3$, (B) epitaxial HEOs transferred via a sacrificial-layer approach, (C) locally epitaxial HEOs grown on oxide nanosheets, and (D) HEOs directly deposited on Pt. To our knowledge such a systematic study of deposition templates and the effect of catalytic activity has not been reported

before. While differences in, for example, crystalline quality are expected depending on the deposition template, the implications for functionality, such as OER performance, remain to be resolved.

We employ standard Si substrates for simplicity, but our approaches (ii)–(iv) can be directly adapted to SiN_x membranes for x-ray- or electron-transparent architectures. Accordingly, these templates provide complementary geometries for advanced mechanistic and operando studies with well-defined structural and interfacial control, and are compatible with a broad range of techniques including environmental TEM [29, 30], pump–probe spectroscopies [31], and spectro-electrochemical microscopy [32, 33]. By comparing their electrochemical behavior and *ex-situ* characterization, including reflective high-energy electron diffraction (RHEED), x-ray diffraction (XRD), transmission electron microscopy (TEM), atomic force microscopy (AFM), and x-ray photoelectron spectroscopy (XPS), we establish how template selection influences the structure and performance of high-entropy oxides grown using an identical pulsed-laser deposition (PLD) recipe. The systematic differences observed across these geometries underscore the critical role of substrate and interface effects in HEO thin-film growth and highlight the importance of deliberate sample design in advanced mechanistic and operando studies.

2. Experimental

2.1. Thin film preparation

$LaNi_{0.2}Co_{0.2}Fe_{0.2}Mn_{0.2}Cr_{0.2}O_3$ thin films were deposited on several deposition templates. $SrTiO_3$ (001) and 0.5 wt% Nb:$SrTiO_3$ (001) (10×10 mm^2, Shinkosha) substrates were etched in buffered hydrofluoric acid and subsequently annealed in oxygen at 950 °C for 75 min to obtain step-terraced surfaces with TiO_2 termination. Silicon wafers (10×10 mm^2) were sputter-coated with a 5 nm Ti adhesion layer and 50 nm Pt and either used directly or after deposition of $Ca_2Nb_3O_{10}$ nanosheets, prepared by the Langmuir–Blodgett method as described in [34, 35].

Thin film depositions were performed by PLD (TSST B.V., The Netherlands) using a mixed-metal $LaNi_{0.2}Co_{0.2}Fe_{0.2}Mn_{0.2}Cr_{0.2}O_3$ target (prepared following [4]) and a $Sr_2CaAl_2O_6$ target (Toshima Manufacturing Co., Ltd). The target–substrate distance was fixed at 50 mm and the laser spot size at 1.8 mm^2. A KrF excimer laser ($\lambda = 248$ nm) was used for ablation. Deposition conditions are summarized in table 1, for the HEO this is an optimized recipe for growth on single crystalline $SrTiO_3$ substrates. The growth was monitored *in situ* using RHEED with a Staib EK-35-R electron source and KSA K-30FW detector, controlled using KSA 400 software (k-Space Associates Inc. USA).

For the film transfer (schematic in SI figure S1), as-grown samples were spin-coated with cellulose acetate butyrate (CAB) (5 g CAB, $M_n \approx 30{,}000$ g mol^{-1}, Sigma Aldrich, dissolved in 100 ml ethyl acetate). Spin coating was carried out with a ramp rate of 1000 rpm s^{-1} to 3000 rpm and hold at 3000 rpm for 1 min. Samples were baked on a hot plate at 150 °C for 2 min to promote adhesion and to remove trapped solvents to get a stable uniform film. The film perimeter was cut with an 11P blade before immersion in water to facilitate water penetration into the sacrificial-layer. After overnight soaking, the CAB-supported film detached and floated to the surface. It was collected onto an oxygen-plasma-cleaned Si \ SiO_2 \ TiO_x \131 Pt substrate and baked again at 150 °C for 2 min to ensure adhesion. The CAB layer was removed by dissolution in ethyl acetate overnight. Lastly, the film is rinsed with isopropanol and blow-dried with nitrogen.

2.2. Physical characterization

XRD was performed using a Panalytical X'Pert PRO MRD (Malvern Panalytical, The Netherlands) equipped with a Cu Kα source and a four-bounce Ge(220) hybrid monochromator.

AFM was carried out in tapping mode on a Bruker Dimension ICON using TESPA-V2 probes (7 nm nominal tip radius) and the data is processed using Gwyddion software [36].

Scanning transmission electron microscopy (STEM) measurements were performed with a Spectra 300 system from Thermo Fisher Scientific on lamellae prepared by FIB with the Thermo Scientific Helios 5 UX DualBeam. Imaging was performed at room temperature with a high angle annular dark field detector and a double tilt holder, at 300 kV, the convergence angle was set to 20 or 30 mrad. Lower convergence angle values are generally known to reduce electron channeling and thus improve the resolution in chemical maps. Here, the lower 20 mrad convergence angle was preferred for the energy dispersive x-ray (EDX) analysis, performed in order to study the chemical composition of the films, while still yielding high resolution STEM images. The EDX set-up comprises a segmented Super-X G2 detector for high solid angle collection of x-rays. The pixel dwell time was kept at only 10–20 µs and the probe current was about 50–60 pA, in order to prevent or limit the local damage during acquisition. The data is analyzed using the Velox software.

Table 1. PLD deposition conditions for $Sr_2CaAl_2O_6$ and $LaNi_{0.2}Co_{0.2}Fe_{0.2}Mn_{0.2}Cr_{0.2}O_3$.

	Fluence (J cm^{-2})	Temperature (°C)	P_{O_2} (mbar)	Frequency (Hz)
SCAO	1.25	750	0.001	2
HEO	1.9	650	0.01	10

XPS measurements were acquired using a SPECS system at the University of Twente [12], with Al Kα excitation and a 20 eV pass energy. The data is analyzed using the CasaXPS software.

2.3. Electrochemical characterization

Electrocatalytic measurements were conducted in a three-electrode configuration in 0.1 M KOH (Sigma-Aldrich, 99.99%), saturated with oxygen. Thin-film working electrodes were mounted on a rotating disk electrode (Pine Research Instrumentation, Inc.) using a custom-made thin-film clamp and Pt sputtering around the sample as described in [11] and rotated at 1600 rpm. A Hg/HgO reference electrode (CH Instruments, CH152), calibrated against a reversible hydrogen electrode (HydroFlex, USA), and a Pt counter electrode were employed. Measurements were performed using a BioLogic SP-300 potentiostat. The measured cyclic voltamograms are normalized to the geometric surface area of 0.442 cm^2 and iR corrected using the R value obtained at the high-frequency intersect of potentiostatic electrochemical impedance spectroscopy measurements at open circuit potential as described in [37].

3. Results and discussion

3.1. Thin film growth

The films are all grown with the same growth recipe (see Experimental section) with the growth tracked using RHEED. Figure 2 presents the RHEED diffraction patterns of the substrates and the subsequently grown layers, along with the corresponding intensity variations observed during growth. In figure 2(A), the Nb:$SrTiO_3$ \ HEO sample shows a RHEED diffraction pattern characteristic of TiO_2-terminated Nb:$SrTiO_3$ [38]. The HEO layer grown on top displays a diffraction pattern with similar in-plane lattice spacing compared to the Nb:$SrTiO_3$, representative of 2D growth mode. Additional weaker diffraction spots appear between the main diffraction features, suggesting a surface reconstruction with a periodicity twice that of the unit cell. The RHEED intensity oscillations confirm a layer-by-layer growth mode, with a total of 25 oscillations directly corresponding to 25 unit cells (u.c.) of HEO deposited on the substrate. The growth rate is ∼40 pulses/u.c., this value is used as a guideline for the other HEO films, which did not exhibit RHEED oscillations, as discussed below.

For the $SrTiO_3$ \ $Sr_2CaAl_2O_6$ \ HEO sample (figure 2(B)), the RHEED diffraction pattern for the substrate and final HEO layer are almost identical to the Nb:$SrTiO_3$ \ HEO sample. The only difference is that a higher filament current was used during acquisition of the HEO film, resulting in more pronounced diffraction spots. However, HEO growth on $Sr_2CaAl_2O_6$ does not exhibit RHEED intensity oscillations, likely due to differences in wetting behavior between HEO on top of $Sr_2CaAl_2O_6$ compared to HEO on top of Nb:$SrTiO_3$ resulting in a different growth mode. The $Sr_2CaAl_2O_6$ film itself shows a RHEED pattern and periodic intensity oscillations indicative of a Sr-deficient $Sr_2CaAl_2O_6$ surface [39]. A total of 2500 pulses were used during growth, resulting in an approximately 18 nm thick $Sr_2CaAl_2O_6$ film, as confirmed by XRD.

Figure 2(C) shows the RHEED results for HEO grown on $Ca_2Nb_3O_{10}$ nanosheets. As expected from the random in-plane orientation of the nanosheets, a clear specular reflection is observed, but no distinct diffraction spots are visible. Instead, faint Laue rings appear. During HEO deposition, no intensity oscillations are observed; however, the overall intensity of the specular spot increases. This increase is likely due to a higher diffraction probability in the HEO thin film, arising from the larger number of scattering planes compared to the ultrathin nanosheet. The growth mode on an individual nanosheet cannot be resolved, as RHEED probes a large surface area, averaging over grain boundaries and multiple nanosheets. After HEO deposition, diffuse 3D diffraction spots appear around the specular spot, which are typically associated with small crystalline particles on the surface. We tentatively attribute these features to a mixed 2D/3D growth mode or to contributions from the regions between nanosheets, where highly textured growth on the exposed Pt layer is expected.

Finally, for direct growth on Pt (figure 2(D)), the substrate shows a strong specular spot with weaker 3D diffraction spots, indicating textured crystalline Pt acting as a growth template for HEO. While oriented or even epitaxial growth of perovskite oxides on Pt(111) facets has been reported under specific

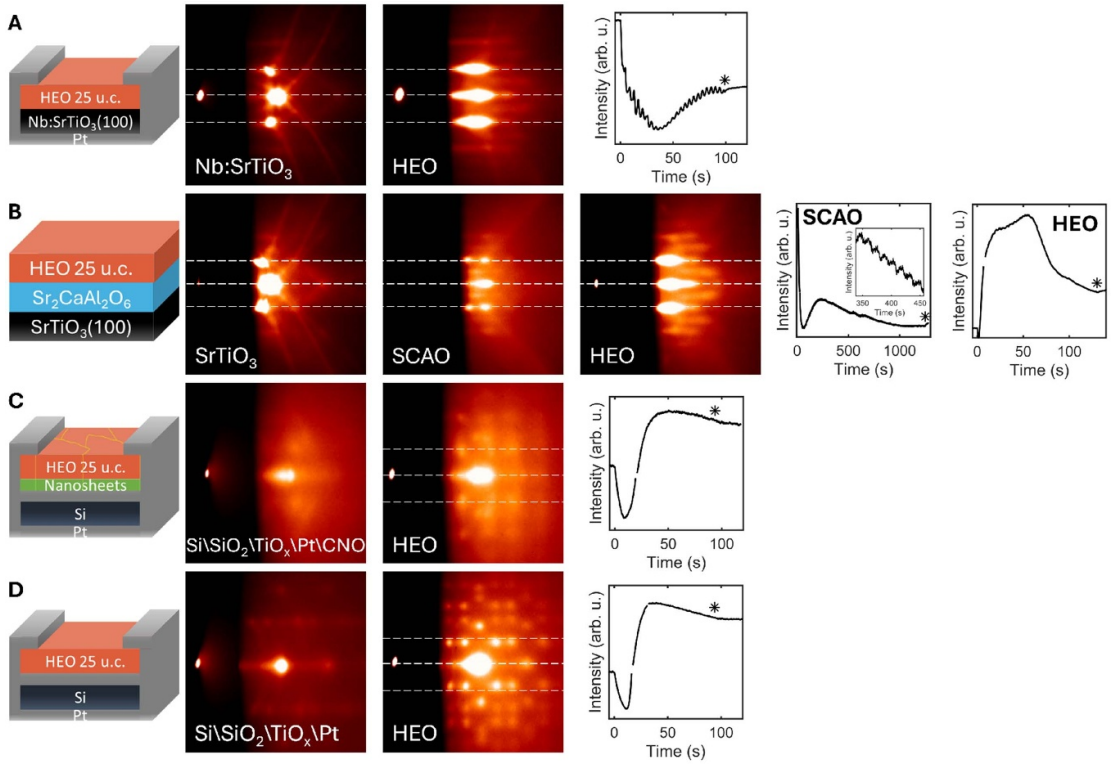


Figure 2. The RHEED pattern and intensity oscillations of (A) Nb:$SrTiO_3$ and HEO, (B) $SrTiO_3$, $Sr_2CaAl_2O_6$ and HEO, (C) $Ca_2Nb_3O_{10}$ and HEO, (D) Pt and HEO. The white dashed lines represent the in-plane reciprocal space distance of the epitaxially grown HEO on Nb:$SrTiO_3$. The * in the intensity evolution graph marks the end of the deposition.

conditions [40], we do not expect well-defined epitaxy of the HEO on the sputter-deposited, textured Pt. Accordingly, the HEO layer shows 3D diffraction spots with a similar pattern as observed for the sample grown on nanosheets; however, the spots are sharper rather than diffuse, indicative of bigger crystalline particles on the surface and a higher coverage of particles with identical orientation. Furthermore, the white dashed lines, representing the in-plane reciprocal-space distances of the epitaxially grown (001)-oriented HEO, do not coincide with the diffraction spots of the HEO films grown directly on Pt. This discrepancy suggests either a different crystallographic plane is exposed or that the film experiences a different strain state, a point to which we will return below. No RHEED intensity oscillations are observed during the growth of HEO on this substrate, in agreement with a 3D growth mode.

To summarize, the HEO growth is layer-by-layer on the Nb:$SrTiO_3$ substrate while different growth modes are observed for growth on $Sr_2CaAl_2O_6$, $Ca_2Nb_3O_{10}$ and Pt. All diffraction patterns indicate crystalline HEO growth, while the growth on Nb:$SrTiO_3$ and $Sr_2CaAl_2O_6$ is 2D, the growth on $Ca_2Nb_3O_{10}$ and Pt is 3D.

3.2. Crystal structure

Figure 3(A) and (B) show the XRD patterns and rocking curves of the HEO films grown on the different deposition templates. In all cases, the HEO$(002)_{pc}$ reflection (pseudo-cubic notation as the bulk $LaNi_{0.2}Co_{0.2}Fe_{0.2}Mn_{0.2}Cr_{0.2}O_3$ has an orthorhombic crystal structure) appears at slightly lower 2θ values than the Nb:$SrTiO_3$ substrate, indicating an out-of-plane lattice parameter almost identical to that of $SrTiO_3$, ≈ 3.9 Å, similar to previous findings [4] and close the bulk lattice parameter of $LaNi_{0.2}Co_{0.2}Fe_{0.2}Mn_{0.2}Cr_{0.2}O_3$ [41]. For the film directly grown on Nb:$SrTiO_3$, pronounced Laue fringes are observed, indicating excellent crystallinity and smooth interfaces. This is consistent with the narrow rocking-curve with a FWHM of 0.115°(the substrate FWHM is 0.0062°[42]). The film grown on $SrTiO_3$ with a $Sr_2CaAl_2O_6$ sacrificial layer also exhibits clear fringes. In this case, two periodicities are visible: the broader-spaced fringes (●) arise from the thinner HEO layer ($\sim$10 nm), while the finer oscillations (⧫) originate from the thicker $Sr_2CaAl_2O_6$ layer ($\sim$18 nm). The layer thicknesses were estimated using a kinematic XRD simulation (not shown), which reproduces the main features of the data and provides a reasonable description of the experimental diffraction pattern.

After transfer onto Pt, the XRD pattern shows a well-defined HEO peak with a single set of fringes and no indication of secondary phases. However, the Si (002) diffraction peak appears, this diffraction

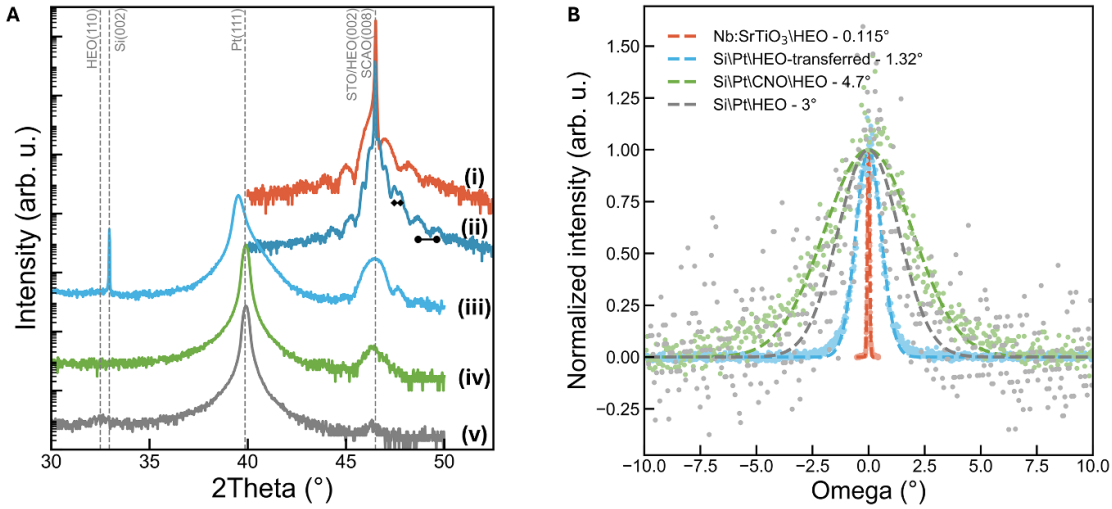


Figure 3. (A) Out-of-plane XRD patterns of HEO (i) on $Nb:SrTiO_3$, (ii) on $SrTiO_3$ \ SCAO (iii) transferred to Si \ SiO_2 \ TiO_x \ Pt, (iv) on Si \ SiO_2 \ TiO_x \ Pt \ $Ca_2Nb_3O_{10}$ and (v) on Si \ SiO_2 \ TiO_x \ Pt. (B) Rocking curve of the samples, dots are the data points and dashed line is a fitted Gaussian function. The FWHM values extracted from the fits are listed in the legend.

condition is only met at specific azimuthal angles [43], and is therefore coincidentally satisfied and not observed in the other samples. The FHWM of the rocking-curve is 1.32°, indicating good but reduced crystalline order compared to the epitaxial film on $Nb:SrTiO_3$. In contrast, the films directly grown on $Ca_2Nb_3O_{10}$ nanosheets and on Pt exhibit much weaker HEO (002) diffraction peaks indicating a lower out-of-plane crystallinity, consistent with their broader rocking curves of 4.7°, and 3°, respectively, or a polycrystalline growth. The sample grown on nanosheets shows a notable (002) peak but no other peaks are evident in the symmetric wide-angle scan (SI figure S2), consistent with locally epitaxial growth directed by the nanosheets. However, the reduced intensity suggests that only part of the film is well oriented, while regions between nanosheets likely grow in a more polycrystalline manner. The growth in these regions is likely similar to the more polycrystalline/textured growth directly on Pt, where only weak $(002)_{pc}$ and $(110)_{pc}$ peaks appear in the symmetric wide-angle scan (SI figure S2). The appearance of these (001) and (110) orientations corresponds well with previous reports of perovskite oxides on Pt [40].

For the samples involving PLD growth on Pt and nanosheet-covered Pt, a shift in the Pt(111) peak can be observed compared to the sample after HEO transfer. This shift is attributed to annealing of the Pt layer during PLD growth, in agreement with previous reports [44]. In contrast, the transferred HEO layer was deposited onto as-prepared, sputter-deposited Pt without further annealing.

In figure 4, TEM images of the HEO and its thicknesses on different deposition templates are shown. On $Nb:SrTiO_3$, perfect epitaxial cube-on-cube growth of the HEO is observed, in agreement with the XRD results, combined with the absence of extended defects like misfit dislocations in the analyzed areas, this suggests near-commensurate epitaxial alignment. The measured thickness is 8.5 nm, slightly below the expected 9.75 nm from RHEED. This discrepancy arises from the TEM lamella being prepared at the corner of the 10x10 mm sample, due to the known thickness gradient in PLD growth [45].

For the transferred film, we observe a mostly intact, dense perovskite structure, closely resembling that of the fully epitaxial stack. While most of the HEO has a thickness of 9.4 nm, some 'pillars' with a diameter of ∼10 nm reach a thickness of ∼14.5 nm; only these pillars appear to be in direct physical contact with the supporting Pt layer. These thickness variations may originate from structural features in the $Sr_2CaAl_2O_6$ layer or from the dissolution process, but were not further investigated in this work. Nevertheless, the catalytic top surface remains comparably well-defined and directly comparable to that of the HEO grown on $Nb:SrTiO_3$, which is the primary focus of this study.

For the HEO on $Ca_2Nb_3O_{10}$, the perovskite crystal structure can still be identified, confirming the local epitaxial growth. This was made possible by intentionally preparing the FIB lamella parallel to a nanosheet edge. The crystallographic orientation is (001) throughout the field of view; however, slight tilting of the lattice planes is observed between different regions, likely due to the flexibility of the nanosheets, which conform to the texture of the Pt substrate and induce locally varying growth directions in the HEO film [46]. The darker contrast between the Pt substrate and the nanosheets is likely caused by the rough Pt surface morphology, with the comparatively smooth nanosheets bridging

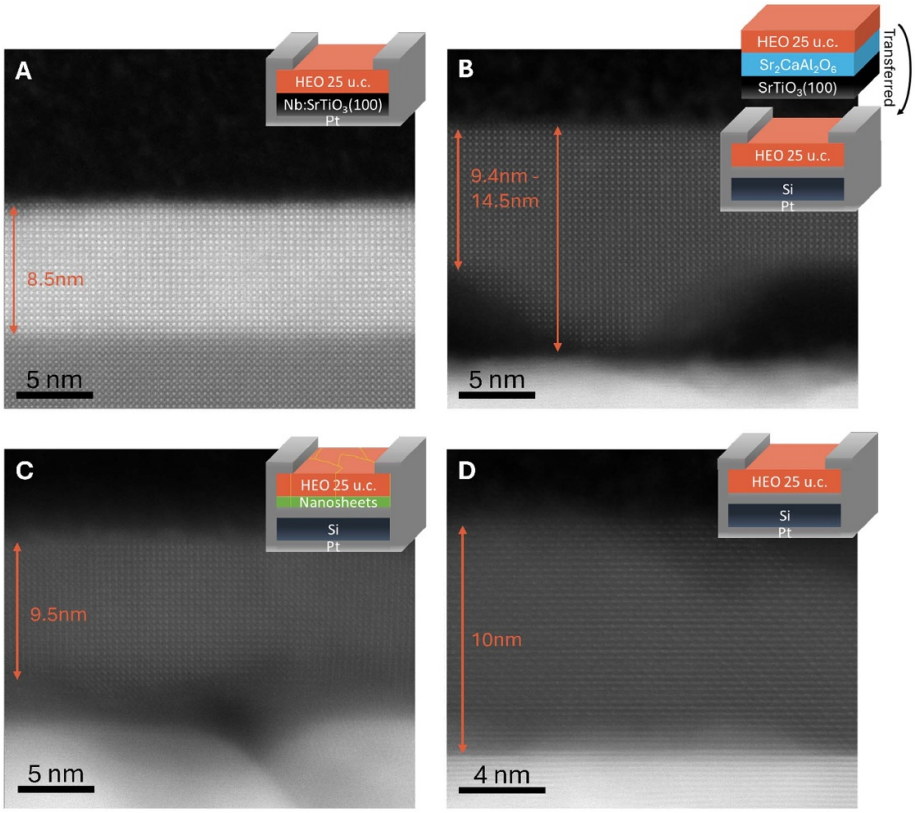


Figure 4. TEM of HEO (A) on $Nb:SrTiO_3$, (B) transferred to Pt, (C) on $Ca_2Nb_3O_{10}$ nanosheets and (D) directly grown on Pt.

adjacent Pt grains. This may result in apparent voids at the interface, although their presence cannot be confirmed with certainty from these measurements. In contrast, the film directly grown on Pt exhibits only limited crystalline periodicity, with no atomic-scale resolution, reflecting the more randomly oriented growth of HEO on Pt and the likelihood of multiple grains being imaged throughout the lamella thickness. Surprisingly, the HEO films on $Ca_2Nb_3O_{10}$ and Pt are slightly thicker than the film grown on $Nb:SrTiO_3$ although the same number of pulses was used. This may be attributed to differences in the growth mode.

These TEM results confirm the XRD analysis: All samples exhibit a perovskite HEO phase with an out-of-plane lattice parameter close to that of $SrTiO_3$, with highest crystalline quality and well-defined epitaxy for the film on $Nb:SrTiO_3$, followed by the transferred film. The films grown on $Ca_2Nb_3O_{10}$ nanosheets and directly on Pt exhibit reduced crystallinity and broader orientation distributions; however, local epitaxial alignment is preserved on the nanosheets, whereas growth on Pt is predominantly textured or polycrystalline.

3.3. Surface morphology

Figure 5 presents the AFM images of the as-grown and transferred HEO films. In figure 5(A), the film grown on $Nb:SrTiO_3$ exhibits a smooth and well-defined surface in which the substrate terrace structure (SI figure S3) remains clearly visible, consistent with the layer-by-layer growth mode and high surface quality evident in the RHEED patterns. The transferred film (figure 5(B)) shows an increased surface roughness with distinct particles scattered across the surface. These features likely arise from residual polymer or other contaminants introduced during the transfer process, since the RHEED patterns before transfer showed no indication of 3D growth, and no post-transfer annealing was performed to remove the organic residues. This ensures that the HEO surface remains as comparable as possible between samples on different deposition templates.

Figure 5(C) shows the morphology of the film grown on $Ca_2Nb_3O_{10}$ nanosheets with a coverage of ~90% (figure SI S3). The underlying nanosheet structure remains recognizable: the film appears smooth at the center of each nanosheet, while increased roughness is observed near nanosheet edges. Larger particles are also present in the regions between nanosheets, suggesting that areas lacking templating support exhibit 3D growth as was also observed in the RHEED. Similar large particles are found on the film deposited directly on Pt (figure 5(D)), consistent with 3D growth observed in the RHEED.

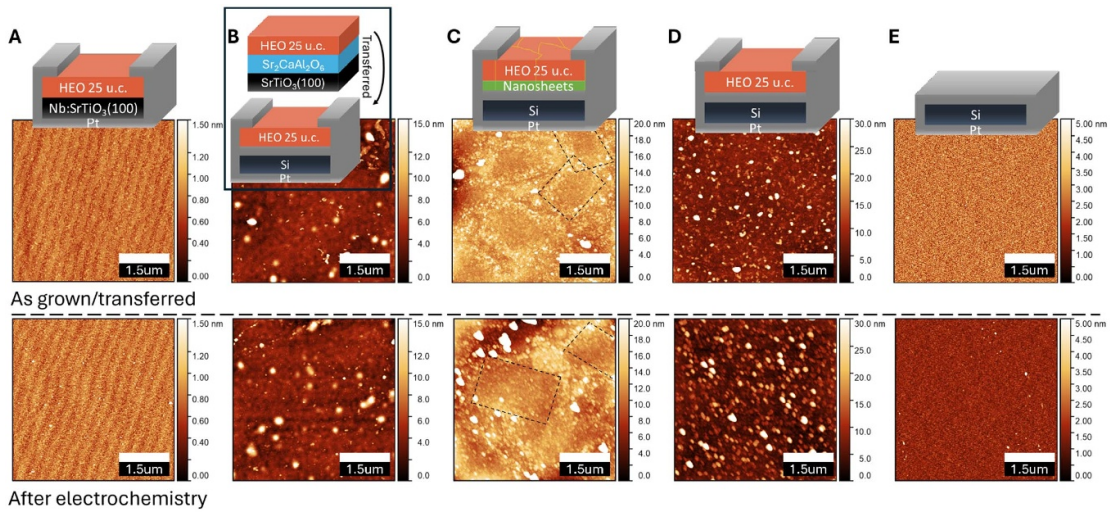


Figure 5. AFM images of the catalyst surface acquired after growth/transfer (top row) and after electrochemical treatment (bottom row) of (A) HEO on $Nb:SrTiO_3$, (B) HEO transferred to Pt, (C) HEO on $Ca_2Nb_3O_{10}$ nanosheets (individual nanosheets remain visible, as indicated by the dashed lines.), (D) HEO directly grown on Pt and (E) $Si \setminus SiO_2 \setminus TiO_x \setminus Pt$. For each sample, the images before and after electrochemistry share the same color scale bar, but the scale varies between samples.

Analogous AFM analysis was performed after the electrochemical treatment described in section 3.5. Post-electrochemistry AFM images (figure 5, bottom row) indicate that the surface morphology is predominantly preserved, with only a slight increase in particle formation observed for the $Ca_2Nb_3O_{10}$ -based and Pt-based samples. For the $Nb:SrTiO_3 \setminus$ HEO sample, slight surface roughening on the step terraces is observed post-electrochemistry. A similar phenomenon has been reported by Verhage *et al* [9], who studied the same HEO composition and likewise observed terrace roughening after electrocatalytic treatment. Finally, figure 5(E) presents AFM images of a $Si \setminus SiO_2 \setminus TiO_x \setminus Pt$ thin film, included as a reference for the template and for comparison with the electrochemical results. In both the pre- and post-electrochemistry images, the film appears smooth, although a few surface particles emerge after electrochemistry.

3.4. Elemental composition

Under optimized growth conditions, pulsed laser deposition can enable nearly stoichiometric transfer of material from the target to the deposited film. However, the compositional complexity of the $LaNi_{0.2}Co_{0.2}Fe_{0.2}Mn_{0.2}Cr_{0.2}O_3$ target, combined with template-dependent variations in surface kinetics, necessitates detailed stoichiometric analysis. Figure 6(A) compares the bulk stoichiometry of HEOs grown on different deposition templates, as determined by EDS (corresponding EDS maps are provided in SI S4–S7). We recorded two EDS maps per sample: one measurement spot before and one after electrochemistry. While this allows direct comparison between samples and before/after electrochemical treatment, the information remains highly local. Overall, we observe roughly the expected 1:1 ratio of the La (50%) and total transition metal concentrations (5× ∼10%), but some variations of the individual transition metal concentrations become apparent. The HEO grown on $Nb:SrTiO_3$, as well as the transferred film, exhibit near-equimolar transition metal compositions, similar to previous reports. In contrast, the HEO films grown on $Ca_2Nb_3O_{10}$ and directly on Pt show a clear deficiency in Ni and Co. This may be attributed to diffusion of these typical alloying elements [47] into the Pt or lower effective sticking coefficient of these elements during deposition on Pt-based templates. Plume-induced nonstoichiometries, for example due to increased scattering, are unlikely, as such effects would also be expected for films grown on $Nb:SrTiO_3$ and $SrTiO_3$.

In addition to the bulk stoichiometry, the surface stoichiometry was determined by XPS, whose surface sensitivity makes it especially suitable for probing electrocatalytic processes such as the OER. Using Al Kα excitation, the total probing depth is ∼7 nm, with a mean information depth of 2 nm [12]. XPS spectra of the transition metal 3p, and La 5 score levels were acquired before and after electrochemical measurements (SI figure S8).

From the XPS compositional analysis based on peak area analysis using relative sensitivity factors (RSFs) (figure 6(B)), the lanthanum-to-transition-metal ratio is shifted toward La (68%), indicating a preferential La-terminated surface. Furthermore, variations in the relative transition metal composition (ranging from 2.5 to 10%) are more pronounced at the surface (XPS) compared to the bulk

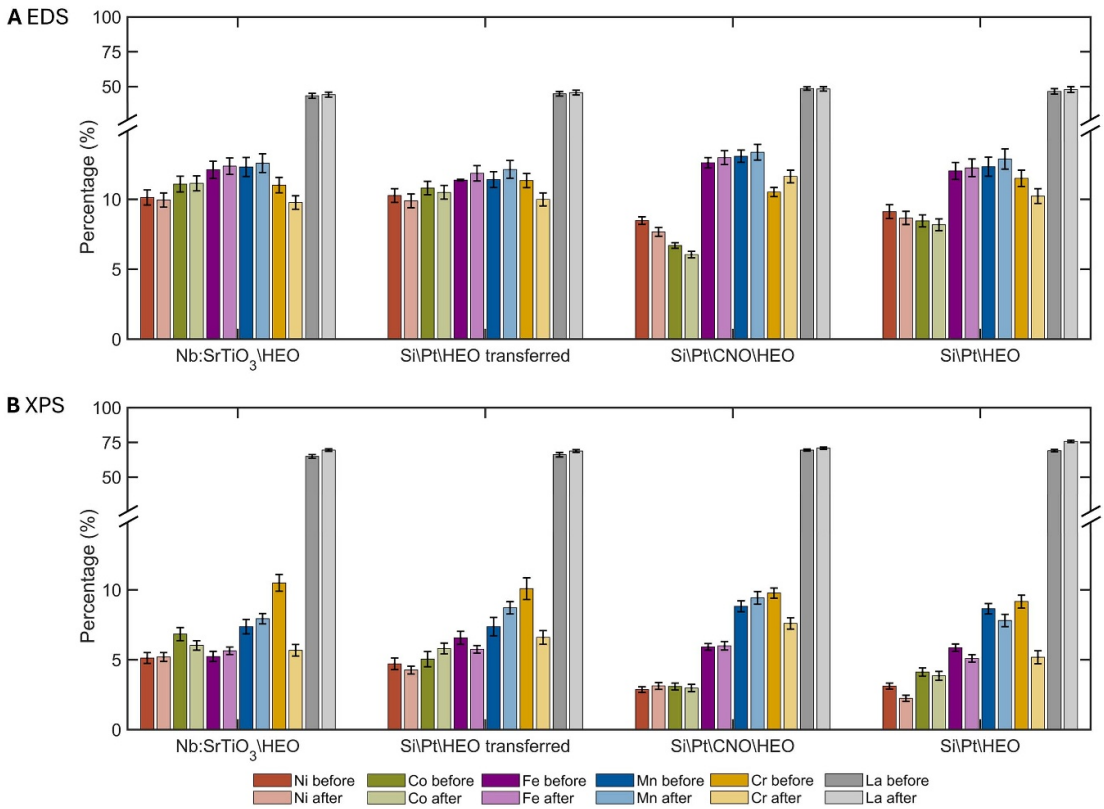


Figure 6. Stoichiometry of the HEOs on different deposition templates. (A) Determined from EDS maps. Error bars represent estimated EDS fitting and quantification uncertainties as determined in the Velox software. (B) Calculated from the XPS transition metal 3p peaks and the La 4d peak. Monte Carlo simulations built into CasaXPS were used to estimate the error bars based on the uncertainties in peak area resulting from random noise in the data. The stoichiometry before and after the electrochemistry is shown in darker and lighter colors, respectively.

(EDS). Consistently, both XPS and EDX show deficiency of Ni and Co in the HEO films grown on the $Ca_2Nb_3O_{10}$ nanosheets and directly on Pt, with a more severe deficiency near the surface (XPS). We note that the absolute compositions obtained from XPS depend on the applied RSF values, derived from the Scofield database and the instrument transmission function, and may therefore carry minor uncertainties beyond the reported error bars. However, the observed trends between different samples remain robust.

After the electrochemical treatment described below, only minor changes are observed in the stoichiometry determined by EDS, indicating that the bulk composition is largely unaffected by OER cycling. In contrast, XPS reveals a pronounced decrease in Cr content during OER treatment across all samples, while only small changes are observed for the other elements (Ni, Co, Fe, Mn, and La). Because of the surface-sensitivity of XPS discussed above, this suggests that Cr leaches from the surface into the electrolyte during electrochemical operation, a phenomenon previously reported for Cr-based electrocatalysts [9, 48, 49].

3.5. Catalytic activity

The OER performance of the HEO on different deposition templates is measured in a rotating disk electrode set-up, as described in the Experimental section. In figure 7(A), the first and fifth cyclic voltammetry (CV) cycles of HEO films on different templates are shown, along with a thin-film Pt reference. All samples exhibit a substantial OER performance, as we have reported before for the fully epitaxial film [4], clearly outperforming the Pt reference film. While all films show a decreased current density with increasing cycle number, clear differences between samples emerge. The transferred HEO film and the film grown on $Nb:SrTiO_3$ display the highest catalytic activity with $\sim$3 mA cm^{-2} at 1.7 V vs. RHE in the fifth cycle, on par with our previous report [4]. In contrast, samples grown on nanosheets and those directly on Pt show lower activity, below $\sim$0.5 mA cm^{-2} at the same potential. Interestingly, the relative performance of the transferred and fully epitaxial films changes between the first and fifth cycle: while the fully epitaxial film shows slightly higher activity at high potentials in the first cycle, both films exhibit comparable activity in the fifth cycle. Furthermore, potentiostatic electrochemical impedance spectroscopy reveals uncompensated resistance of the different samples in a reasonable range. Hence,

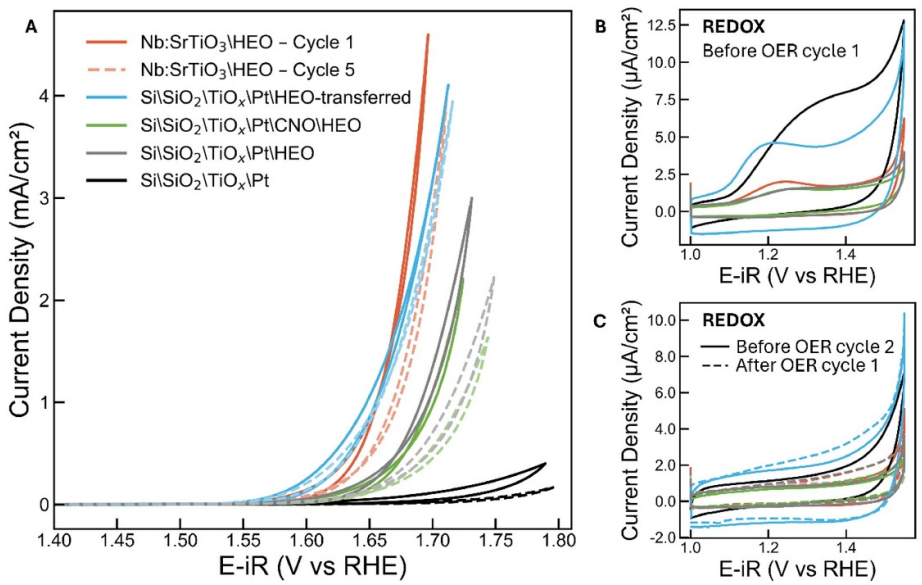


Figure 7. (A) Cyclic voltammetry curves (first and fifth cycles) of the HEO films on the different deposition templates, including a Pt thin-film reference, shown with a focus on the OER potential region. (B) Cyclic voltammetry in the redox potential region for cycle 1 prior to OER cycling. (C) Cyclic voltammetry in the redox region for cycle 2 prior to OER cycling and for cycle 1 following OER cycling. A sweeprate of 10 mV s^{-1} is used.

activity differences do not originate from iR correction (SI figure S9). Likewise, double-layer capacitance measurements before and after OER cycling show no significant changes for any of the HEO samples (SI figure S10), suggesting that differences in activity cannot be attributed to major changes in electrochemically accessible surface area. Given the limited statistics, we therefore consider their activities to be similar within experimental uncertainty.

The observed electrocatalytic performance correlates with crystallinity, as reflected by the FWHM of the rocking curves. Films with higher crystalline quality, namely those grown on Nb:$SrTiO_3$ and the transferred sample, exhibit the highest activity, whereas films with reduced crystallinity show lower activity. In addition to crystallinity, compositional differences may also play a role for the activity: the more active samples exhibit near-equimolar transition metal concentrations, while the films on $Ca_2Nb_3O_{10}$ and Pt show reduced Ni and Co contents, especially at the catalytically active surface, which coincides with their lower activity.

To further assess differences between samples, we compare their behavior in the so-called redox regime at potentials below the OER onset, where transition metal oxidation and reduction peaks have been observed before, e.g. the pronounced Ni oxidation and reduction near 1.4 V vs. RHE [10]. Figures 7(B) and (C) display CV scans collected in the so-called redox regime, performed before (solid line) the OER and after (dashed line) the OER cycling experiment. In figure 7(B), the first cycle reveals a distinct oxidation peak at approximately 1.2 V vs. RHE for the HEO films, while the broad Pt oxidation peak emerges at around 1.3 V. No reduction peaks are observed in this potential window. In contrast, from the second cycle onward before OER, as well as in all subsequent cycles collected after OER cycling (figure 7(C)), no discernible redox features are observed. Since only a single oxidation peak is present, this feature is most likely associated with elemental dissolution. XPS reveals a pronounced decrease in Cr content; therefore, we attribute this oxidation peak to Cr dissolution. However, there is no clear correlation in dissolution peak area from electrocatalysis and Cr loss by XPS, suggesting a complex dissolution process which will be addressed in future work. Interestingly, Cr dissolution is most pronounced for the most active samples (NbSTO-grown and transferred) and less pronounced for the less active samples (deposited on CNO nanosheets and directly grown on Pt). This suggests that Cr leaching may be beneficial for the OER activity of the HEO. However, a full understanding of this trend and its relation to OER mechanisms would require operando characterization.

Lastly, the transferred film exhibits a higher double-layer capacitance compared to the other samples. This may be attributed to a larger electrochemically active surface area (ECSA), as microscopy images (SI figure S11) reveal a rougher surface morphology characterized by wrinkles. Furthermore,

slight delamination and crack formation are observed after electrocatalysis, which may allow limited electrolyte penetration between the Pt substrate and the transferred film, thereby increasing the ECSA.

To summarize, HEOs grown on Nb:$SrTiO_3$ and the transferred films exhibit the highest catalytic activity, along with near-equimolar transition metal stoichiometry and superior crystallinity, characterized by a single exposed crystal facet. However, the surface morphology indicates the presence of residual polymer contamination, which might affect the OER performance. In contrast, samples deposited directly on Pt and on $Ca_2Nb_3O_{10}$ nanosheets show similar but reduced activity, accompanied by lower crystallinity. Nevertheless, HEOs grown on nanosheets maintain a preferred orientation and exhibit a more defined surface morphology, with fewer particles compared to films grown directly on Pt. Furthermore, XPS and EDS analysis reveal significant Ni and Co deficiencies relative to the nominal equiatomic composition, which correlates with the reduced catalytic activity observed in these less crystallinefilms.

4. Conclusion

In this work, we demonstrate the deposition of HEOs on a range of deposition templates. Specifically, we investigate HEOs grown on Nb:$SrTiO_3$, $Ca_2Nb_3O_{10}$ nanosheets, and directly on Pt with epitaxially grown films subsequently transferred to Pt. The resulting crystal quality, stoichiometry, and morphology vary substantially depending on the chosen template. We found that HEO films grown on Nb:$SrTiO_3$ and transferred films have the best crystallinity (highly oriented single phase) and close to equiatomic stoichiometry, yielding the highest OER performance. In contrast, HEO films grown on $Ca_2Nb_3O_{10}$ nanosheets and directly on Pt result in reduced crystalinity, Ni and Co deficiency, and lower OER performance.

These results highlight that direct comparison of HEO films grown on different templates, even under identical growth conditions, inevitably yields significant differences in crystallinity, morphology, and elemental composition, leading to variations in electrochemical performance. Therefore, for operando spectroscopic studies and model-system catalyst design, films grown on transferred substrates and on Nb:$SrTiO_3$ currently provide the most comparable platforms with the highest catalytic activity. However, further investigation is required to better understand and potentially improve the interface between the transferred films and the Pt back-contact [50]. In particular, a systematic annealing study could provide insight into the role of post-growth annealing in modifying the interface. Additionally, annealing may help remove polymer residues observed by AFM, thereby improving film quality. As an additional pathway towards model systems, growth on $Ca_2Nb_3O_{10}$ nanosheets may be further improved by incorporating an additional $SrTiO_3$ buffer layer, which could enhance film quality [51], although this may simultaneously alter electronic transport properties due to the insulating nature of $SrTiO_3$. Nevertheless, with a careful buffer layer choice, nanosheet-based approaches offer a viable pathway toward near-ideal model systems.

More broadly, these findings emphasize that systematic model studies should ideally be conducted within a single, well-defined deposition template. Switching between different templates introduces additional variables that significantly impact catalytic behavior, thereby complicating direct comparisons. If comparison across different growth templates is nevertheless required, for example, to enable operando spectroscopies or other specialized measurement techniques, then growth recipes must be individually optimized for each template, this could potentially optimize the crystallinity, stoichiometry and electrochemical activity. In such cases, careful *ex situ* characterization is essential to verify structural, morphological, and compositional similarity, ensuring that the samples can be used in a truly complementary manner. Furthermore, these approaches are not limited to HEO catalysts, but are equally applicable to other perovskite and spinel oxide electrocatalysts.

Acknowledgments

We thank Christian B. I. van Weerdenburg for assisting with AFM and XRD measurements, Mohana V. Kante for target manufacturing and Lasse Wichman for sputtering of the Pt contacts for the electrochemistry.

Data availability statement

The data that support the findings of this study are openly available at the following URL/DOI: https://doi.org/10.4121/bf417440-0c43-4fba-844a-32d20dcc8f63 [52].

Supplementary Information available at https://doi.org/10.1088/2515-7639/ae7d59/data1.

Funding

We greatfully acknowledge funding from the European Union (ERC, 10 104 0669 - Interfaces at Work). The opinions and perspectives presented are solely those of the author(s) and do not necessarily align with the views of the European Union or the European Research Council. Neither the European Union nor the funding authority bears responsibility for the content expressed. Part of this research was carried out at the MESA+ operando HAXPES user facility at the University of Twente. This publication is part of the project 'Lab-based HAXPES facility for operando studies of energy-material interfaces' with file NO: 175.2019.001 of the research programme NWO-groot 2019/2020 which is (partly) financed by the Dutch Research Council (NWO).

Author contributions

Iris C G van den Bosch 0009-0004-6249-8729
Conceptualization (lead), Data curation (lead), Formal analysis (lead), Investigation (lead), Methodology (lead), Project administration (lead), Resources (lead), Software (lead), Supervision (lead), Validation (lead), Visualization (lead), Writing – original draft (lead), Writing – review & editing (lead)

Martina Tsvetanova
Investigation (equal), Resources (equal), Validation (equal), Writing – review & editing (equal)

Melissa J Goodwin 0000-0002-2803-9789
Investigation (equal), Resources (equal), Validation (equal), Writing – review & editing (equal)

Edwin Dollekamp 0000-0001-8956-5785
Methodology (equal), Resources (equal), Validation (equal), Writing – review & editing (equal)

Nini Pryds 0000-0002-5718-7924
Methodology (equal), Resources (equal), Supervision (equal), Validation (equal), Writing – review & editing (equal)

Gertjan Koster 0000-0001-5478-7329
Conceptualization (equal), Funding acquisition (equal), Methodology (equal), Resources (equal), Supervision (equal), Validation (equal), Writing – review & editing (equal)

Christoph Baeumer 0000-0003-0008-514X
Conceptualization (equal), Funding acquisition (lead), Methodology (equal), Resources (equal), Supervision (lead), Validation (equal), Writing – review & editing (equal)

References

[1] Löffler T, Ludwig A, Rossmeisl J and Schuhmann W 2021 *Angew. Chem. Int. Edn* **60** 26894–903
[2] Banko L, Krysiak O A, Pedersen J K, Xiao B, Savan A, Löffler T, Baha S, Rossmeisl J, Schuhmann W and Ludwig A 2022 *Adv. Energy Mater.* **12** 2103312
[3] Nguyen T X, Liao Y C, Lin C C, Su Y H and Ting J M 2021 *Adv. Funct. Mater.* **31** 2101632
[4] Kante M V *et al* 2023 *ACS Nano* **17** 5329–39
[5] Svane K L 2025 *Curr. Opin. Electrochem.* **51** 101670
[6] Kiens E M, Choi M J, Wei L, Lu Q, Wang L and Baeumer C 2023 *Chem. Commun.* **59** 4562–77
[7] Weber M L and Gunkel F 2019 *J. Phys. Energy* **1** 031001
[8] Adiga P and Stoerzinger K A 2022 *J. Vac. Sci. Technol. A* **40** 010801
[9] Verhage M, Broek v d S J, Weijtens C and Flipse C F J 2025 *ACS Appl. Mater. Interfaces* **17** 23237–48
[10] Füngerlings A, Wohlgemuth M, Antipin D, van der Minne E, Kiens E M, Villalobos J, Risch M, Gunkel F, Pentcheva R and Baeumer C 2023 *Nat. Commun.* **14** 8284
[11] Baeumer C *et al* 2021 *Nat. Mater.* **20** 674–82
[12] van den Bosch I C G, Zaman J U, Shterk G, Hamed M H, Schneider M, Ratovskii V, Bu Y, Dietrich P M, Koster G and Baeumer C 2025 *Sci. Adv.* **11** eadw6673

[13] Axnanda S, Crumlin E, Mao B, Brown G E, Ellis T, Liu Z and Bluhm H 2015 *Sci. Rep.* **5** 9788
[14] Barawi M, Mesa C A, Collado L, Villar-García I J, Oropeza F, de la Peña O'Shea V A and García-Tecedor M 2024 *J. Mater. Chem. A* **12** 23125–46
[15] Nemšák S, Strelcov E, Duchoň T, Guo H, Hackl J, Yulaev A, Vlassiouk I, Mueller D N, Schneider C M and Kolmakov A 2017 *J. Am. Chem. Soc.* **139** 18138–41
[16] Velasco-Vélez J J *et al* 2021 *J. Appl. Phys.* **54** 124003
[17] Che Q *et al* 2024 *J. Phys. Chem. C* **128** 5515–23
[18] Che Q, van den Bosch I C G, Ruiters J R H, Piao Y, Baeumer C, Glatzel P, Kühn D and de Groot F M F 2026 *J. Am. Chem. Soc.* **148** 414–24
[19] Shalom B O, Andrés M A, Yu Y, Head A R and Eren B 2022 *Electrochem. Commun.* **142** 107375
[20] Timmerman M A, Xia R, Le P T P, Wang Y and ten Elshof J E 2020 *Chem. Eur. J.* **26** 9084–98
[21] Chiabrera F M, Yun S, Li Y, Dahm R T, Zhang H, Kirchert C K R, Christensen D V, Trier F, Jespersen T S and Pryds N 2022 *Ann. Phys., Lpz.* **534** 2200084
[22] Lu D, Baek D J, Hong S S, Kourkoutis L F, Hikita Y and Hwang H Y 2016 *Nat. Mater.* **15** 1255–60
[23] Choo S, Varshney S, Liu H, Sharma S, James R D and Jalan B 2024 *Sci. Adv.* **10** eadq8561
[24] Harbola V, Xu R and Hong S S 2025 *Adv. Phys. X* **10** 2450538
[25] Zhang J *et al* 2024 *Science* **383** 388–94
[26] Brand E *textitet al* 2025 *ACS Nano* **19** 41172–83
[27] Mandal R, Yun S, Wurster K, Dollekamp E, Shondo J N and Pryds N 2025 *Nano Lett.* **25** 5541–9
[28] Li Y *et al* 2022 *Adv. Mater.* **34** 2203187
[29] Su D 2017 *Green Energy Environ.* **2** 70–83
[30] Benavidez A D, Kovarik L, Genc A, Agrawal N, Larsson E M, Hansen T W, Karim A M and Datye A K 2012 *ACS Catalysis* **2** 2349–56
[31] Lazemi M 2025 In the blink of an x-ray: femtosecond x-ray absorption of transition metal perovskites *Doctoral Thesis* (Utrecht University) chapter 5: deciphering femtosecond spin dynamics in textured $LaFeO_3$ thin films (https://research-portal.uu.nl/en/publications/in-the-blink-of-an-x-ray-femtosecond-x-ray-absorption-of-transiti/
[32] Lim J *et al* 2016 *Science* **353** 566–71
[33] Mefford J T *et al* 2021 *Nature* **593** 67–73
[34] Yuan H, Nguyen M, Hammer T, Koster G, Rijnders G and ten Elshof J E 2015 *ACS Appl. Mater. Interfaces* **7** 27473–8
[35] Yuan H, Lubbers R, Besselink R, Nijland M and ten Elshof J E 2014 *ACS Appl. Mater. Interfaces* **6** 8567–74
[36] Nečas D and Klapetek P 2012 *Cent. Eur. J. Phys.* **10** 181–8
[37] Heymann L *et al* 2025 *ACS Appl. Mater. Interfaces* **17** 21110–21
[38] Koster G 1999 Artificially layered oxides by pulsed laser deposition *PhD Thesis* Research, Graduation University of Twente Netherlands (available at: https://ris.utwente.nl/ws/portalfiles/portal/6076180/t0000012.pdf)
[39] Sun H, Zhang C, Song J, Gu J, Zhang T, Zang Y, Li Y, Gu Z, Wang P and Nie Y 2020 *Thin Solid Films* **697** 137815
[40] Panomsuwan G, Takai O and Saito N 2014 *Appl. Surf. Sci.* **309** 95–105
[41] Sarkar A, Djenadic R, Wang D, Hein C, Kautenburger R, Clemens O and Hahn H 2018 *J. Eur. Ceram. Soc.* **38** 2318–27
[42] Shinkosha Co., Ltd 2012 *$SrTiO_3$ (Strontium Titanate) Substrate Technical Report (Shinkosha Co., Ltd. Yokohama, Japan product catalog / technical datasheet)*(available at: www.shinkosha.com/english/wp-content/uploads/sites/2/2023/05/SrTiO3_eng.pdf) (Accessed 2 June 2026)
[43] Hwang B H 2001 *J. Phys. D. Appl. Phys.* **34** 2469
[44] Gruber W, Baehtz C, Horisberger M, Ratschinski I and Schmidt H 2016 *Appl. Surf. Sci.* **368** 341–7
[45] Avila R A, Kiens E, Birkhölzer Y, Shanker O, Coolman T, Struik M, Bu Y, Baeumer C, Rijnders G and Koster G 2025 *J. Cryst. Growth* **668** 128313
[46] Birkhölzer Y A 2022 *PhD Thesis* Nanoscale strain control of oxide thin films Research, graduation University of Twente Enschede (available at: https://ris.utwente.nl/ws/portalfiles/portal/282244831/Birkholzer2022_NanoscaleStrainControlOfOxideThinFilms.pdf)
[47] Greeley J, Stephens I E L, Bondarenko A S, Johansson T P, Hansen H A, Jaramillo T F, Rossmeisl J, Chorkendorff I and Nørskov J K 2009 *Nat. Chem.* **1** 552–6
[48] Luo S, Dai C, Ye Y, Wu Q, Wang J, Li X, Xi S and Xu Z J 2024 *Angew. Chem. Int. Edn* **63** e202402184
[49] Malek A, Xue Y and Lu X 2023 *Angew. Chem.* **135** e202309854
[50] Kp H *et al* 2026 *Adv. Mater.* **38** e21189
[51] Nunnenkamp M, Perez D, Smithers M, Houwman E, Rijnders G and Koster G 2024 *Thin Solid Films* **790** 140190
[52] Van den Bosch I C G, Martina M, Melissa M J, Dollekamp E, Pryds N, Koster G and Baeumer C 2026 Data underlying the publication: effect of deposition template on high entropy oxide model systems for the oxygen evolution reaction *4TU.Research Data* (https://doi.org/10.4121/bf417440-0c43-4fba-844a-32d20dcc8f63)